communications earth & environment

ARTICLE

https://doi.org/10.1038/s43247-021-00204-9 OPEN

Accounting for tropical cyclones more than doubles the global population exposed to low-probability coastal flooding

Job C. M. Dullaart [1✉], Sanne Muis [1,2], Nadia Bloemendaal [1], Maria V. Chertova[3], Anaïs Couasnon[1] & Jeroen C. J. H. Aerts [1,2]

Storm surges that occur along low-lying, densely populated coastlines can leave devastating societal, economical, and ecological impacts. To protect coastal communities from flooding, return periods of storm tides, defined as the combination of the surge and tide, must be accurately evaluated. Here we present storm tide return periods using a novel integration of two modelling techniques. For surges induced by extratropical cyclones, we use a 38-year time series based on the ERA5 climate reanalysis. For surges induced by tropical cyclones, we use synthetic tropical cyclones from the STORM dataset representing 10,000 years under current climate conditions. Tropical and extratropical cyclone surge levels are probabilistically combined with tidal levels, and return periods are computed empirically. We estimate that 78 million people are exposed to a 1 in 1000-year flood caused by extratropical cyclones, which more than doubles to 192 M people when taking tropical cyclones into account. Our results show that previous studies have underestimated the global exposure to low-probability coastal flooding by 31%.

[1] Institute for Environmental Studies (IVM), Vrije Universiteit Amsterdam, Amsterdam, The Netherlands. [2] Deltares, Delft, The Netherlands. [3] Netherlands eScience Center, Amsterdam, The Netherlands. ✉email: job.dullaart@vu.nl

Driven by strong winds and low pressures in tropical cyclones (TCs) and extratropical cyclones (ETCs), storm surges may threaten coastal areas, especially when they coincide with high tides[1]. Globally, approximately 100 million people live in areas below the current high tide lines[2]. As a consequence, a substantial portion of the socio-economic activity and critical infrastructure is exposed to coastal flooding[3,4]. Examples of recent high-impact storm surge events with their maximum surge level and overall losses include TCs Dorian (Bahamas; 7.0 m; $5.1B)[5] and Michael (United States; 4.3 m; $25.0B)[6] and ETCs Xaver (northern Europe; 3.5 m; $1.4B)[7] and Ophelia (Ireland; 1.7 m; $1.0B)[8]. TCs generally form over warm tropical waters and affect regions such as Southeast Asia, the Caribbean, and North Australia[9], while ETCs dominate in the mid-latitudes and affect regions such as South America, Europe, and South Australia. In addition, there are regions that experience both storm systems, including the west and east coasts of Australia (±30°S)[10,11], eastern China (±35°N)[12], and the east coast of the United States (±40°N)[13,14].

Return periods of storm tides (RPs), defined as the combination of storm surge and tide, can provide highly valuable input to flood hazard and flood risk assessments[15,16]. RPs are often used as design standards for the construction of coastal levees and other flood protection measures[17]. On continental to global scales, studies have used RPs to model coastal flooding[18–20] and societal risks under future scenarios of sea-level rise and socio-economic development[21–25].

All global-scale studies on storm tide RPs have inaccuracies in TC-prone regions[18,19,26,27]. The cause of this inaccuracy is two-fold: (1) TCs are poorly resolved due to the coarse spatial and temporal resolution of meteorological forcing data, causing an underestimation in TC intensity and, consequently, storm surge level; and (2) in combination with the low-probability of TCs[28], the limited record length of the meteorological forcing data (typically 40 years)—with ±90 TCs forming per year and only 16 of these making landfall[29]—means the number of TCs is too small to robustly estimate RPs. In addition, TCs affect a relatively small stretch of coastline[30], which reduces the number of recorded TC-induced storm surges. Recent advances in climate modeling, such as the newly developed ERA5 climate reanalysis dataset, have improved the modeling of TC storm surges[31]. However, ERA5's record length of several decades is too short for a robust estimation of high RPs in TC-prone regions[11,14,15].

To overcome these limitations, regional studies on TC storm surges have extended the historical TC record by generating synthetic TC tracks[32–34]. These synthetic TC tracks, representing thousands of years of TC activity, are generated through statistical resampling and modeling of observed TC tracks and intensities. The main advantage of such a method is that it does not assume an upper tail behavior based on an extreme value fit, which can be unstable with a limited sample size. Instead, low exceedance probabilities are estimated empirically from the large set of reconstructed events. Such approaches have been applied in places like Australia[10,11], The United States[35], New York[13,14], Tampa, Cairns, and the Persian Gulf[36]. More recent, global-scale studies have built on these regional approaches and developed new synthetic TC datasets, enabling RP estimates for up to 10,000-years[28,37,38] with high statistical confidence. These novel datasets pave the way to properly account for TC-induced storm surges and compute more robust storm tide RPs on a global scale. However, a global-scale study on storm tide RPs using synthetic TC tracks has never been conducted.

This study addresses this research gap by presenting a new combined global dataset of TC and ETC storm tide RPs that we call COAST-RP (COastal dAtaset of Storm Tide Return Periods). Building upon the hydrodynamic modeling framework presented in prior research[18,26,39], our methodology contains two main novelties. First, TC-induced and ETC-induced storm surges are modeled separately using different types of meteorological forcing. For TCs we use synthetic TC tracks from the STORM dataset[28]. STORM is a fully statistical model that extracts the TC characteristics from any input dataset, in this case, IBTrACS (1980–2017), and statistically resamples this to the equivalent of 10,000 years under the same climate scenario. For ETCs we use the ERA5 climate reanalysis. With ETC storm surges we refer to all surges not caused by a TC. As a result, ETCs are the main drivers of extremes in the ETC surge level time series, though they also include extremes generated by other weather phenomena such as depressions, anti-cyclonic storms, monsoons, and polar lows[40,41]. Second, the extreme value analysis (EVA) method consists of an empirical approach based on a large sample size rather than fitting extreme value distributions and extrapolating storm tide levels to high RPs. To accomplish this, we generate stochastic storm tide event sets based on the possible combinations of tides and surges from TCs and ETCs. This allows for estimations of rare storm tide RPs with high statistical confidence that produce a consistent global dataset with storm tide RPs. Finally, we show how the full inclusion of TCs changes the exposure of the global population to low-probability coastal flooding.

Results

TC storm surge RPs. The 25-year return period (RP25) of TC-induced storm surges exceeds 2.0 m in several regions (Fig. 1a), including the Yellow Sea and East China Sea (China), the Gulf of Carpentaria (Australia), the Bay of Bengal (Bangladesh), and the gulf and east coasts of the United States. For this, we simulate TC storm surges by forcing the Global Tide and Surge Model (GTSM)[26] with 3000 years of the current climate (1980–2017) synthetic TC tracks from the STORM dataset[28] (see "Methods" section). Subsequently, we apply the Weibull plotting position formula to the simulated TC storm surge levels and estimate RPs (Supplementary Fig. 1). To compare the STORM-based results against historical events, we force GTSM with the same TC tracks that were used as input for the STORM model. These TCs are filtered from IBTrACS[9] by selecting those TCs with maximum wind speeds equal to or larger than 18 m s^{-1}, that form within a TC basin and within a TC season (see ref. [28] for an overview). This amounts to 2710 historical TCs in the period 1980–2017. Differences in RP25 surge levels between STORM and IBTrACS are smaller than 0.25 m for 85% and 0.10 m for 67% of the output locations prone to TCs (Fig. 1b). In the Gulf of Mexico, the east coast of the United States, parts of northern Australia, and Madagascar, the difference in RP25 is larger than 0.5 m. However, the 90% confidence interval of STORM RP25 also exceeds 0.5 m in those regions with large differences between the STORM-based and IBTrACS-based RP25 (i.e., at 24% of the output locations). This suggests that at least part of the difference between the synthetic and observed TCs is explained by the stochastic nature of TCs where the 38-year period of IBTrACS can contain too many (or few) or too extreme (or weak) storm surge events compared to the probability of a certain TC storm surge event based on STORM. An example of a storm surge event with a much higher RP than 38 years is TC Sandy, which made landfall near New York and has an estimated storm tide RP of 260 years[14]; this emphasizes the need for a long time series of TC storm surge levels in order to accurately compute RPs.

ETC storm surge RPs. The RP25 for ETC-induced storm surge levels exceeds 2.0 m along with parts of the coastline of Argentina, Uruguay, Australia, and countries bordering the Arctic Ocean and the North Sea (Fig. 2a). To compute ETC RPs we use 38 years

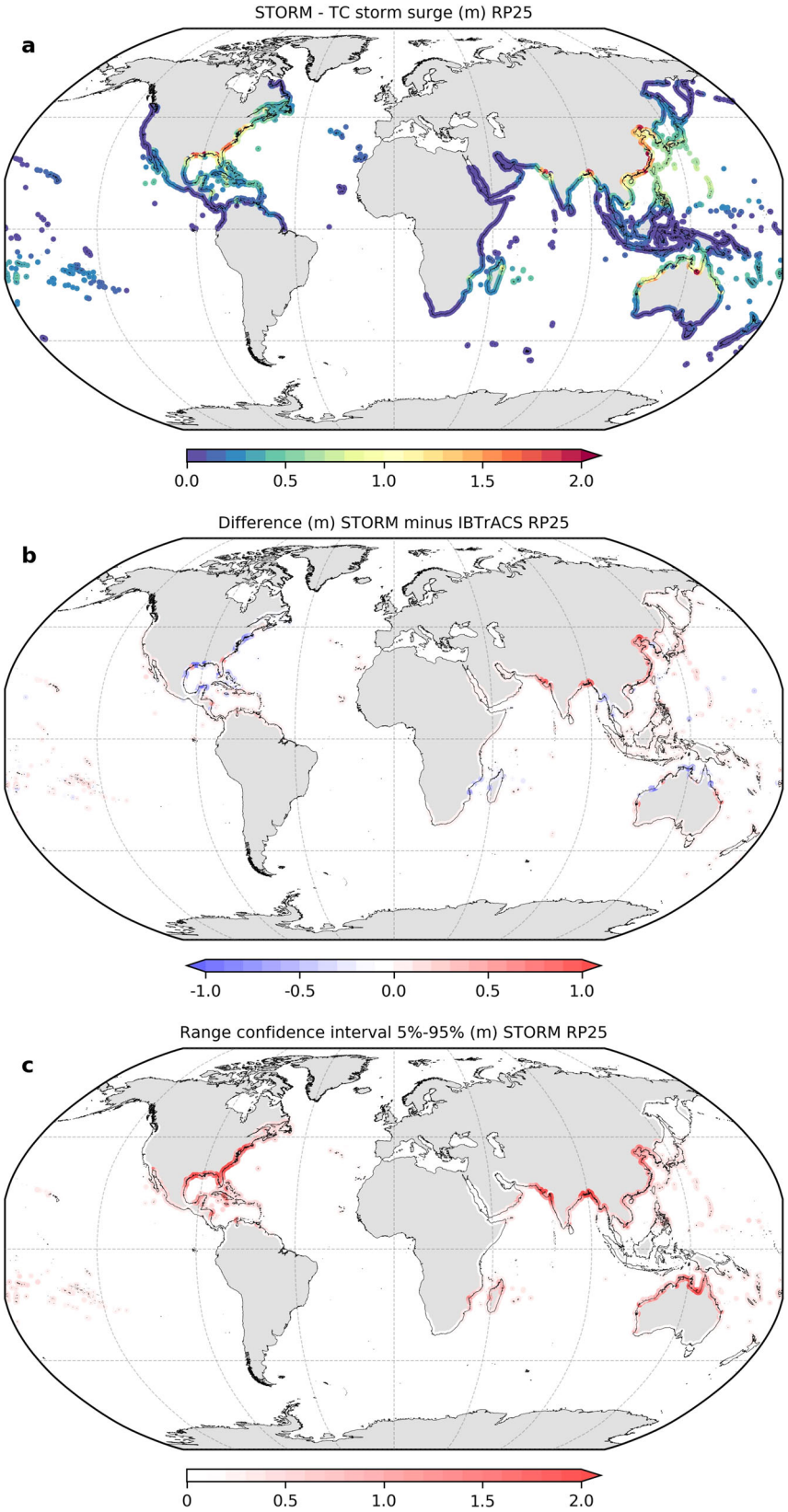

Fig. 1 Tropical cyclone-induced storm surge levels with a 25-year return period. The panels show the (**a**) STORM-based 25-year tropical cyclone storm surge return period, (**b**) absolute difference (m) in TC storm surge levels between STORM and IBTrACS, and (**c**) the range of the 90% confidence interval (m) of STORM. The difference in surge level is calculated by subtracting the IBTrACS-based RPs from STORM; the range of the confidence interval is calculated as the difference between the 5th and 95th percentile.

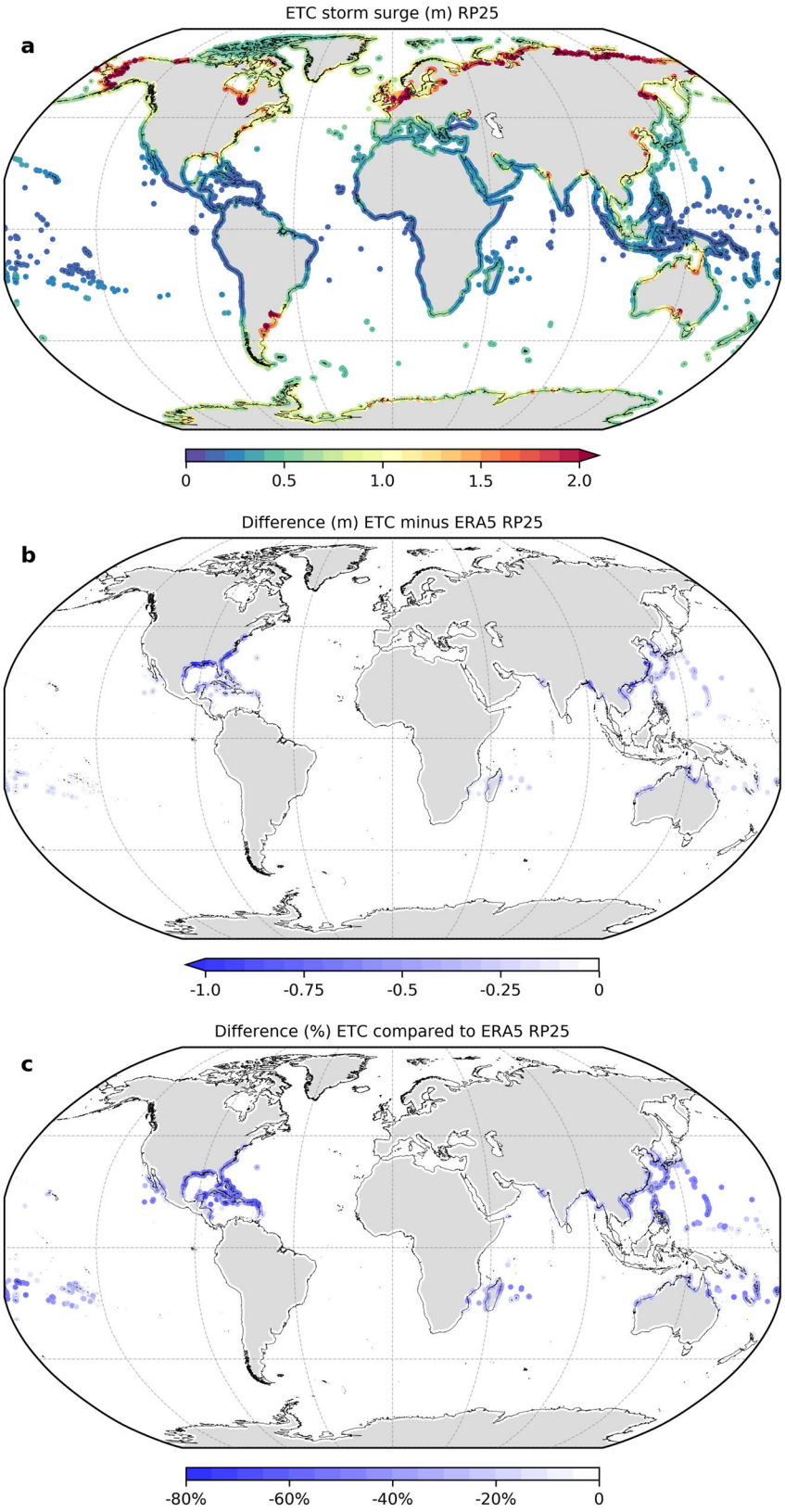

Fig. 2 Extratropical cyclone-induced storm surge levels with a 25-year return period. The panels show the (**a**) 25-year extratropical cyclone storm surge return period, (**b**) absolute difference (m) in surge levels between ERA5 and ETC, and (**c**) the relative difference (%) in surge levels between ERA5 and ETC. The absolute and relative differences in surge level are calculated for the ETC-based RPs relative to ERA5, where ETC is similar to ERA5 but with the tropical cyclones removed.

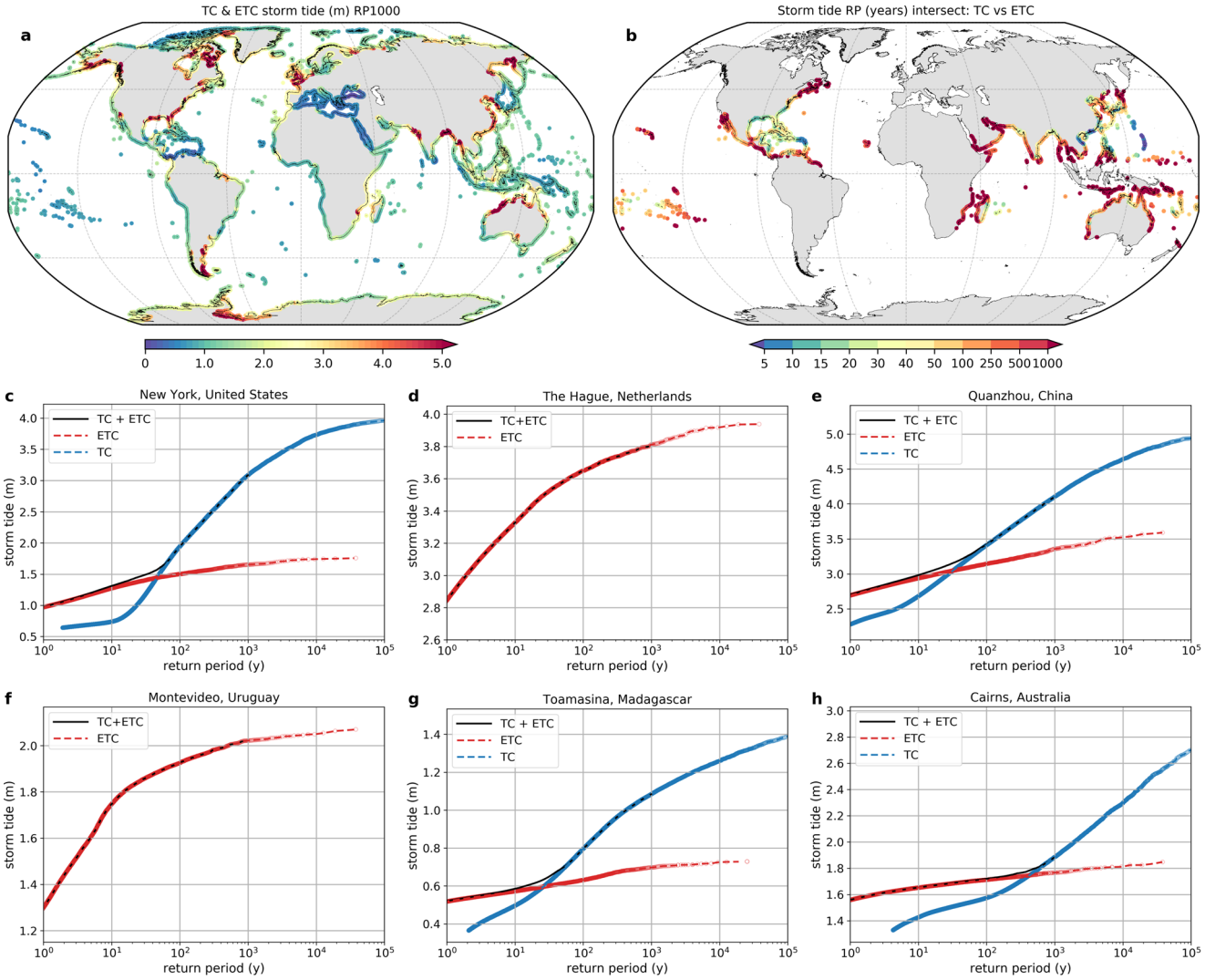

Fig. 3 Storm tide level return periods. The panels show the (**a**) 25-year storm tide return period, (**b**) crossover return period at which tropical cyclones start to exceed extratropical cyclone storm tide levels, and Weibull's plot showing tropical (blue) and extratropical cyclone (red) storm tide return periods, together with the sum (black), at (**c**) New York, (**d**) The Hague, (**e**) Quanzhou, (**f**) Montevideo, (**g**) Toamasina, and (**h**) Cairns.

(1980–2017) of storm surge levels from a prior study[26], which forced GTSM with the ERA5 climate reanalysis. To prevent the double-counting of TCs included in synthetic TC simulations, we remove all TC-induced storm surges from the ERA5 surge levels before calculating ETC storm surge RPs (see "Methods" section). The effect of removing TC storm surges from the ERA5 surge levels on the RP25 surge level (Fig. 2b) is especially large in eastern China, north Australia, and the United States' gulf and east coasts with reductions of up to 1.0 m. This result is in line with the RP25 for TC storm surges, which shows the highest surge levels in the same regions. The relative effect (Fig. 2c) is large (>50%) in the previously named regions, as well as islands in the Caribbean, Pacific, and South Indian Oceans. These islands are affected by TCs infrequently, while ETCs generally do not occur in such tropical regions; this explains the large relative decrease in storm surge level.

Global storm tide RPs. At 3% of the output locations the RP1000 storm tide level exceeds 5.0 m (Fig. 3a), particularly in areas with a shallow and wide continental shelf. To obtain storm tide levels at a given location, we combine the TC and ETC surge levels with 1000 random tidal levels taking seasonality into account (see "Methods" section). Subsequently, the RPs of TC-induced and ETC-induced storm tides are computed separately and then probabilistically combined to determine the corresponding RPs. Storm tide levels exceeding 5.0 m are observed on all continents but with different forcing mechanisms. For example, in the Bay of Bengal and the Gulf of Mexico, TCs are the main drivers, while a large tidal range and ETC storm surges are responsible for high storm tides in Europe and Canada. In north Australia and the east coast of The United States, high storm tides are typically caused by the coincidence of a TC or ETC with high tide. In regions with both TCs and ETCs, ETCs influence most low RPs. RPs during which TC storm tide levels surpass those caused by ETCs (Fig. 3b) are low (<10 years) along parts of the coastline of Vietnam, south-east China, northern Philippines, and several islands in the North Pacific and the Caribbean. Typically, RPs beyond which the TC storm tides are larger increase further away from the most TC-active regions, towards the equator and the poles. In general, the RP curve of TC storm tide levels has a steeper slope than the RP curve of ETCs (Fig. 3c-h). Near Quanzhou (China), both TCs and ETCs can produce a substantial storm tide level. As a result, the difference in slope between the RP curves representing TC-induced and ETC-induced storm tides is relatively small, and the TC-ETC transition is smoother

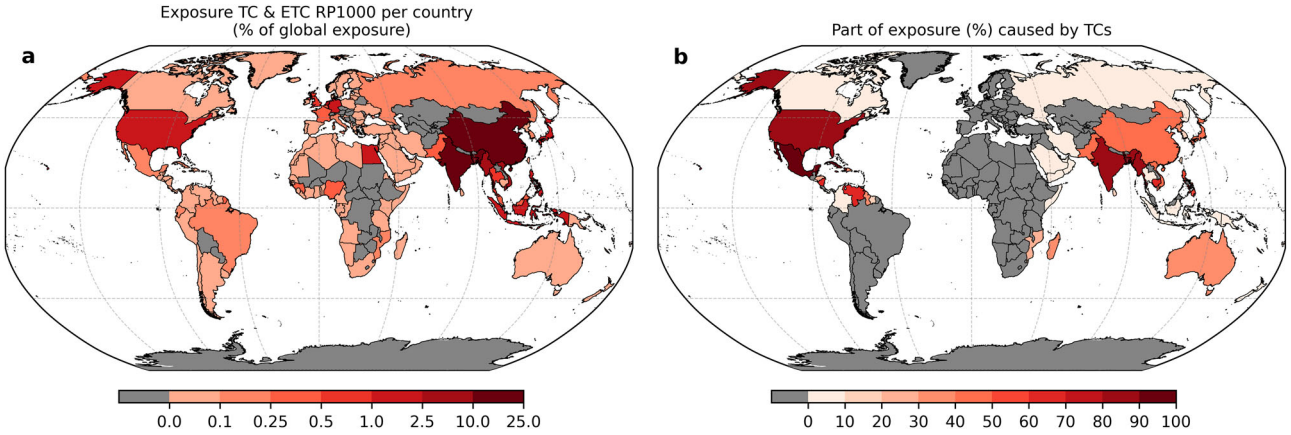

Fig. 4 Exposed population. The panels show the (**a**) number of people exposed to an RP1000 flood event per country relative to the global population, taking TCs and ETCs into account, and (**b**) the part of the exposure caused by TCs per country. For countries depicted in gray on both subpanels, estimates of exposure are equal to zero, while countries that are only gray on the right panel (**b**) are not affected by TCs that contribute to the country's exposure.

than others, like the one in New York (United States). In New York, ETCs referred to as Nor'easters[42], are the main source of RP10 storm tides[14,43]. From RP45, storm tides are dominated by TCs, which can generate substantially higher storm tides compared to ETCs at this location. The transition point, at which the influence of TCs and ETCs is equal in terms of the combined RP, shows the value of quality estimates of TC and ETC storm tide RPs. It is interesting that along the northeast coast of the United States the transition point is approximately RP100, as the 100-year flood zone is used by the National Flood Insurance Program to determine who has to pay flood insurance and who can choose to pay in the United States[14,44]. Finally, in Cairns (Australia), TC-induced storm tides surpass those caused by ETCs at RP391, showing how important it is to consider TCs when estimating high RPs of storm tides, also if TCs are very rare compared to ETCs[36].

To validate the COAST-RP dataset, we compare storm tide RPs with regional studies that use a similar approach along the coastlines of Australia[10,11] and the United States[14,35]. In general, the comparison shows a good agreement. For the RP1000 storm tide levels across 600 output locations in Australia, the root mean square error (RMSE), mean relative bias, and Spearman's rank coefficient are, respectively, 0.60 m, +2.9%, and 0.94. A possible explanation for the positive bias is the higher resolution of GTSM (2.5 km) compared to the grid used by ref. [10] (10 km). ref. [35] presented storm tide RPs in the United States, only taking TCs into account. As COAST-RP indicates that the RP1000 for TC storm tides surpass those induced by ETCs along the east coast of the United States, the results can be compared. The RMSE, mean relative bias and Spearman's rank coefficient based on 23 output locations are, respectively, 0.90 m, +5.8%, and 0.76. The relatively small contribution of tides to storm tides along the United States coastline compared to Australia's could explain the lower Spearman's rank coefficient. For all 23 output locations, our RP1000 storm tide levels fall within the 5th–95th percentiles as reported by ref. [35]. Furthermore, one study[14] assessed both TC and ETC storm tides for the New York area and estimated that TC storm tide levels surpass those of ETCs at a 60-year RP at The Battery, while we find a crossover RP of 45 years. Overall, the validation indicates good agreement of the COAST-RP dataset with regional studies.

Flood exposure. Using a static flood model, we find that 77.8 million people globally are exposed to the ETC RP1000 flood level. This increases to 191.6 million people when taking TCs into account (Fig. 4). This equals, respectively, 1.0% and 2.5% of the global population (Table 1). The estimates of the exposed population are based on MERIT[45] elevation data and the GPWv4[46] population for the year 2020. We assume no protection from coastal flooding because protection standards are below RP1000 along most global coastlines[47]. The exposure per country to TC and ETC RP1000 flood levels relative to the global exposure (Fig. 4a) is especially large in Bangladesh (24%), India (19%), China (14%), and Vietnam (7%). This is a result of their large populations, as well as the high RP1000 storm tide levels exceeding 3.0 m along most of the coastlines of these countries, even exceeding 10.0 m in the Bay of Bengal. Excluding the impact of TCs (Supplementary Fig. 2), the relative exposure is largest in China (17%), followed by the Netherlands (12%), Vietnam (10%), and India (9%). The relative contribution of TCs to total exposure per country, relative to ETCs, is especially large (>90%) in Puerto Rico, Belize, Cuba, Mexico, and Bangladesh (Fig. 4b); additionally the United States and India are highly exposed to TC-induced flooding. To explore which countries with small populations may be hit hard by an RP1000 flood event, we also calculate the exposure per country relative to the country's population (Table 1). This way, countries with a small number of inhabitants

Table 1 Top ten countries exposed to RP1000 flood levels.

	Absolute exposure (×1 million people)		Relative exposure (% of country population)
Country	Total (% TC)	Country	Total (% TC)
Bangladesh	46.3 (91%)	Netherlands	55.9 (0%)
India	37.0 (80%)	Bahamas	43.2 (62%)
China	25.9 (49%)	Bangladesh	28.4 (91%)
Vietnam	13.6 (46%)	Myanmar	15.7 (84%)
Netherlands	9.4 (0%)	Vietnam	14.3 (45%)
Myanmar	8.8 (84%)	Guyana	10.5 (38%)
Indonesia	4.6 (0%)	Belgium	7.4 (0%)
United States of America	3.7 (86%)	Greenland	6.4 (0%)
Japan	3.5 (46%)	Guinea	5.2 (0%)
Philippines	2.9 (55%)	Albania	3.9 (0%)
World	191.6 (59%)	World	2.5 (60%)

The table shows the exposure to RP1000 flood levels for the top ten most exposed countries. Countries are ranked by estimates of absolute (left two columns) and relative exposure (right two columns) to RP1000 flood levels. Here, relative exposure indicates the number of people flooded per country relative to the country's population. The number between brackets indicates the contribution of TCs to the total exposure as a percentage.

are also listed in the top 10 most exposed countries, such as the Bahamas and Guyana (population <1.0 million).

By combining ETCs from ERA5 and TCs from STORM, the COAST-RP dataset provides a major improvement compared to the previous datasets[18,19,26], which have not fully accounted for the low probabilities of TCs. Here we compare results against previous exposure estimates using the same flood model. The RP1000 flood map based on the COAST-RP dataset results in a 31% higher exposure estimate compared to the RP1000 flood map from ref. [25], which used the GTSR[18] dataset and IBTrACS[9]-based TC simulations as input. Countries where the exposed population at least doubles are those known to face TCs, for example, Myanmar, the Bahamas, Japan, and the United States. For lower RPs (RP < 1000) it differs whether the exposure estimate is largest using COAST-RP or Aqueduct[48] (Supplementary Table 1). More specifically, for RPs below RP10 or above RP100 the COAST-RP-based exposure estimate is higher compared to Aqueduct. Note that these differences are not simply the effect of including TCs but are the aggregated effect of the higher resolution input data and model, as well as the use of other statistical methods. However, the large difference for high return periods does indicate that previous studies have underestimated the global exposure to coastal flooding by not fully accounting for low-probability TCs.

Discussion

This study provides a novel global dataset of storm tide RPs, COAST-RP, that for the first time includes low-probability TCs. By using synthetic TCs from the STORM dataset and sampling the surge with random tides we were able to estimate storm tide RPs without fitting a parametric extreme value distribution. Our global modeling framework gives comparable results to studies that applied a similar approach at smaller spatial scales. The exposure analysis showed that 78 million people are exposed to the ETC RP1000 flood level, which increased to 192 million people when taking TCs into account. In addition, the exposure estimate based on the COAST-RP RP1000 flood map is 31% higher compared to Aqueduct[48], which is based on the GTSR dataset[18] and TC tracks from IBTrACS[9]. This indicates that previous studies have greatly underestimated the global exposure by not fully accounting for low-probability TCs.

Several aspects of our methodology could be improved. First, the statistical resampling techniques underlying the STORM dataset do not account for physical characteristics[28]. The STORM algorithm allows TCs to propagate within a 5° × 5° box based on the distribution of historical TC tracks in that box. For some locations, this resolution is too coarse, and longer records of observed TCs are required to better train the algorithm. As a result, in some areas there may be too many and too strong or too few and too weak TCs, resulting in an overestimation or underestimation of TC-induced surge levels. For example, in the northwest area of the Pacific, between 30° and 40° latitude, TCs tend to move toward the north or northeast[9]. However, TCs in the STORM dataset also moved westward into the shallow and semi-enclosed Bohai Sea. As a result, modeled TC storm surges of up to 6.5 m largely exceeded the highest observed storm surges of 2.5 m[12,49]. By applying a bias correction at output locations where the IBTrACS-based TC storm surge level RPs fall outside the 5th–95th percentiles of STORM (see "Methods" section), we largely removed this bias. That said, it is inevitable that some overestimations or underestimations of storm tide RPs in TC-prone regions remain in the COAST-RP dataset.

Second, we used the Holland parametric wind model to simulate wind and pressure fields for synthetic TCs. The Holland model assumes that a TC has a symmetric eye with wind speeds reducing away from the eye in a uniform way[50–52] and that it adds asymmetry to the wind field by taking the translational speed of a TC into account. In reality, TCs are much more complex systems where asymmetry is steered by other processes as well[53]. Although this has not a large effect on the highest surge levels that occur near the TC's eyewall, surge levels further away from their centers may be underestimated[54,55]. The application of more advanced parametric wind models[51,56,57] is expected to improve the accuracy of TC-induced storm surges, however, unfortunately, the synthetic TCs from STORM does not contain sufficient information to do so.

Third, our modeling approach simplifies some of the coastal processes. We did not consider tide-surge interactions, wave setup, coastally trapped waves, and mean sea-level variability. Due to computational constraints, tides and surges are modeled separately and probabilistically combined to obtain storm tide levels. Tide-surge interactions are known to be important in areas with a large tidal range and shallow bathymetry[58]. Along most of the global coastline non-linear tide-surge interactions reduce total water levels[59]. Therefore, ignoring the tide-surge interaction component will result in an overestimation of the flood risk in some areas[60]. This could be improved in the modeling framework by, for instance, including the dependence between surge and tidal level. We do account for seasonality as tides are sampled from the month when the surge occurs. Wave setup can increase storm tide levels near the coast, especially in regions with steep slopes[61]. As such, it is often an important component of extreme sea levels, and further developing our modeling framework to also include a dynamic wave component would be a relevant avenue for future research. To accomplish this, we could build upon the work of previous global studies that have applied a parametric approach, using offshore wave height, to obtain estimates of wave setup on a global scale[19,62]. Coastally trapped waves can generate a storm surge that travels far away (>1000 km) from a TC in regions like western Australia and Vietnam[63,64]. These waves are not captured by GTSM as this would require a 3D hydrodynamic model. However, we believe the influence on our results is small as these waves generally do not exceed a few tens of centimeters and only become of interest when they coincide with the actual storm surge. Last, GTSM is a 2D barotropic model and as such we ignore mean sea level variability that is not driven by wind or atmospheric pressure[65]. Driven by steric changes and ocean circulation, mean sea levels vary at seasonal to decadal timescales. This effect can be up to 10 cm which adds to the occurrence of extremes[66].

The COAST-RP dataset provides an improved basis for large-scale flood risk assessments. By using synthetic TCs representing 3,000 years of data, this dataset represents a substantial improvement over existing global datasets, such as the Coastal Dataset for the Evaluation of Climate Impact (CoDEC)[26] and others (e.g., refs. [18,19]). Overall, we expect this to lead to higher estimates of present-day flood risk in TC-prone regions, especially in areas where the historical record includes too few or too weak TC events. In future research, we aim to apply the presented modeling framework to future scenarios and assess the impact of climate change on storm tide RPs. While sea-level rise may be the dominant driver[19], TCs and ETCs are projected to become more intense in some areas. More specifically, most climate models indicate an increase in average TC intensity[67] and project an average 5% increase in lifetime maximum surface wind speeds. In addition, the number of slow-moving TCs is expected to increase[35,68], possibly resulting in prolonged coastal flooding. For ETCs, most climate models show a spatial shift of storm tracks, with a poleward shift in the Southern Hemisphere, for example, but do not indicate a clear change in ETC intensity[69,70]. When combining such information on future storminess with

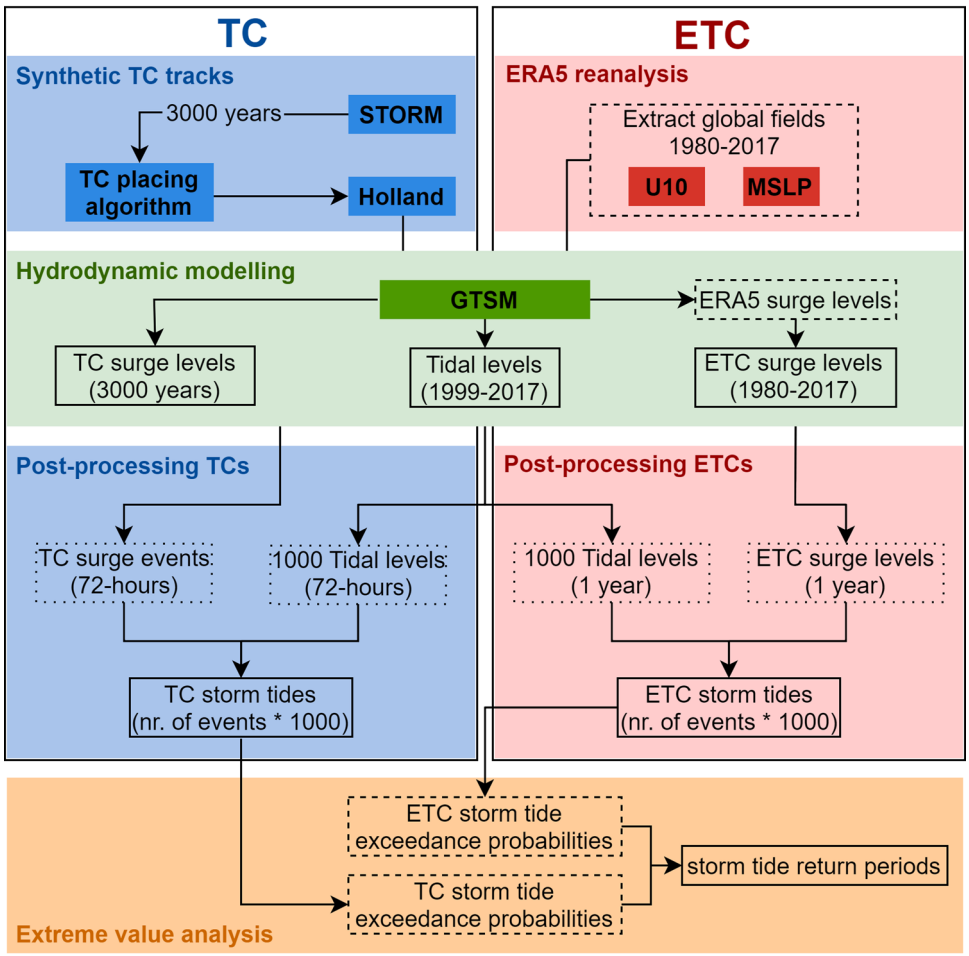

Fig. 5 Modeling framework. Flowchart showing the hydrodynamic modeling (green), and post-processing and extreme value analysis procedure (orange) for each output location. ETC storm tide RPs are computed for each output location (red), and TC storm tide RPs are only included in TC-prone regions (blue).

probabilistic projections of SLR along the coastline of the United States, ref. [35] found that the historical RP100 will occur at least every 30 years toward the end of the 21st century in the southeast Atlantic and the Gulf of Mexico. Such information on future-climate storm tide RPs is essential to accurately assess future flood risk and may prioritize adaptation efforts in areas facing the highest flood risk.

Methods

General approach. Storm tides are driven by the combined effect of storm surges and tides. To estimate the RPs of storm tides, we followed three main steps (Fig. 5). First, we separately simulated TC surge levels, ETC surge levels, and tidal levels. Second, at each output location, we stochastically combined TC and ETC surge levels with random tidal levels to obtain TC and ETC storm tide levels, respectively. Third, we calculated the exceedance probabilities for TC and ETC storm tides using Weibull's plotting position formula[71] and probabilistically combined the two to obtain storm tide RPs.

Hydrodynamic model. Storm surges and tidal levels were simulated with the third generation Global Tide and Surge Model (GTSMv3.0)[26,72]. The GTSMv3.0 is a global depth-averaged hydrodynamic model based on the Delft3D Flexible Mesh software[73]. The resolution varies between 25 km in deeper parts of the ocean and 2.5 km along the coast (1.25 km for Europe). Storm surges can be simulated by forcing GTSMv3.0 with wind and pressure fields. The stress exerted by the wind on the ocean was parameterized by multiplying the quadratic 10-m winds (U10) with the atmospheric density and a user-defined wind drag coefficient (Cd), which depends on the surface roughness[74,75]. Tides were induced by including tide-generating forces using a set of 60 frequencies. The physical processes of internal tides and self-attraction and loading were implemented in GTSMv3.0[72]. To include the 18.6-year nodal cycle, tidal levels were simulated with GTSM for the 1999–2017 period (19 years). Here, we used the same model setup as described in ref. [26], which consisted of 23,226 output locations every 25 km along the global coastline. A subset of 10,641 output locations located in regions prone to TCs was used for simulating TC storm tides. The GTSM forced with ERA5 meteorological data has been validated in previous studies for both RPs of storm tides[26] and individual TC events[31].

TC storm surge modeling. To simulate TC-induced storm surges, we used a dataset of synthetic TC tracks generated with the Synthetic Tropical cyclOne geneRation Model (STORM)[28]. The STORM dataset was created by statistically resampling climatological data from 38 years of best-track historical data found within the International Best Track Archive for Climate Stewardship (IBTrACS)[9]. It was used to generate TCs representing 10,000 years of data under present-climate conditions. Variables extracted from STORM are U10, mean sea level pressure (MSLP), longitude, latitude, and the radius to maximum winds (Rmax). Hydrodynamic simulations conducted using GTSM are computationally expensive; therefore, we used different strategies to reduce the total runtime. First, from the 10,000 years of TC activity in STORM, we only simulated 3000 years of surge levels, which is sufficient to reliably estimate the RP1000[76]. Second, we only used TC tracks that come within 750 km of land. Third, for each TC, we selected the part of the track within 1000 km of the coast. Last, we simulated multiple TCs simultaneously, resulting in another 70% reduction of the total runtime. To make that happen we used a newly developed algorithm that optimizes the spatiotemporal placing of TCs[77]. To prevent a TC from being affected by any other TC, we set a minimum distance of 2000 km between TC tracks.

For each TC track, wind speed, wind direction, and pressure fields were derived using Holland's parametric wind model[50]. The TC fields were represented by a polar grid with 36 radials, 375 arcs, and a 750 km radius. As the global median values of the azimuthally-averaged radius of 12 ms^{-1} winds and outer radius of historical TCs are 197 km and 423 km[78], respectively, a 750 km radius will include all wind speeds capable of generating a significant storm surge[79]. As recommended by ref. [54], the counter-clockwise rotation angle was set at $\beta = 20°$, and the storm

translation to surface background wind reduction factor was set at $\alpha = 0.55$. An empirical surface wind reduction factor (SWRF) of 0.85 was used to adjust the wind fields at gradient levels to 10-m surface levels[80]. A wind conversion factor of 0.915 was applied to convert winds from 1 min average to 10 min average[81]. The inflow angle from ref. [82] was used to measure inward from the azimuthal direction, which increased linearly from 0° at the storm center to 10° at Rmax. Then, the inflow angle increased further to 25° at 1.2 × Rmax and remained at 25° beyond. We used Garrat's drag formula for 10-m wind speeds[83] with $Cd = (0.75 + 0.067U10) \times 10^{-3}$, which has been applied in numerous surge modeling studies[54,84]. Cd is capped at $Cd = 2.5 \times 10^{-3}$ following ref. [85], as most studies agree that Cd begins to level off at wind speeds above 30 ms^{-1} [86]. The final product consisted of TC storm surge time series at a 10-min interval, representing 3000 years of TC activity.

Next, we applied a bias correction to the TC storm surge levels based on TC storm surge levels for observed TCs. The reason for applying a bias correction is that the synthetic TCs in STORM is too intense in some regions, resulting in storm tide RPs that are too high. The bias correction is based on three steps. First, we simulated observed TC-induced storm surges by forcing GTSM with TC tracks from IBTrACS. Missing Rmax values in the IBTrACS dataset were computed based on the latitude and U10 of a TC, using estimates of TC geometry parameters per basin[87]. Second, we computed the 5th and 95th percentiles (i.e., 90% confidence interval) for the STORM RPs based on bootstrapping using 599 repetitions. Per output location, we computed the average storm surge level with an RP between 2 and 19 years for IBTrACS and selected those output locations where the IBTrACS value fell outside the 90% confidence interval of STORM (supplementary Fig. 3). Last, at the selected locations, we multiplied all TC storm surge levels with a correction factor (Supplementary Fig. 4) equal to the average 5th (when too low) or 95th (when too high) percentile value divided by the average IBTrACS value. We used this rather conservative linear scaling method, based on the 5th or 95th percentile instead of the 50th percentile, because IBTrACS itself may underestimate or overestimate the exceedance probabilities due to its limited record length. In most regions where a bias correction has applied the magnitude of the bias correction is negligible. The three main regions where a substantial correction factor is applied include the northeast coast of China (0.7), north Australia (1.4), and the northern coastline of South America (0.6), with the average correction factor in these regions indicated between brackets. Along the northeast coast of China the overestimation of TC storm surges can be explained by the fact that in STORM, TC intensification and weakening are modeled as a function of sea-surface temperature[28]. As a result, a TC can continue to intensify in mid-latitude regions as long as the sea surface temperature is high enough to sustain a TC, whilst in reality, the TC will experience effects from enhanced wind shear and extratropical transition. The underestimation in north Australia is caused by the fact that this region is located near two TC basin boundaries of STORM. Since TCs in STORM are cut off when they cross the basin boundary, this drives an underestimation of TC storm surges in the coastal region near Darwin. Last, the overestimation along the northern coastline of South America may be explained by the additional error term that is applied by the STORM model to simulate a TC track. This error term may cause the TC to move southward as opposed to the much more general north(westward) direction of observed TCs in these latitudinal regions.

ETC storm surge modeling. To simulate ETC-induced storm surges, we made use of wind and pressure fields from the ERA5 climate reanalysis[88] from the European Center for Medium-range Weather Forecasts (ECMWF). ERA5 has a horizontal resolution of 0.25° × 0.25° and a temporal resolution of one hour. The ERA5-based time series of storm surge levels were taken from Muis et al.[26]. We used the 1980–2017 period for two reasons: (1) this period was used to generate the STORM dataset. By using the same period, we ensured that the underlying climate conditions of the TC and ETC simulations were the same; and (2) to prevent the double counting of TCs, we removed the TC-induced storm surges from the ERA5 simulations using IBTrACS, which is complete from 1980 onwards when reliable satellite observations became available. We assume that a storm surge is induced by a TC when there is a TC within 250 km, until 48 h after the last available time step of a TC track. TCs with a Rmax exceeding 50 km is likely to affect a larger stretch of coastline. Therefore, we used a distance of 5 × Rmax if the Rmax exceeds 50 km. A constant Charnock parameter was applied with a value of 0.041[89] to translate wind speed into wind stress[90]. The final product consisted of 38 years of ETC storm surge time series at a 10-min interval.

Extreme value analysis. For TCs, we first detected all surge peaks that are at least three days apart to ensure independent events and we extracted surge levels from 24 h before until 48 h after the peak. Second, a 72-h tidal levels time series was randomly sampled from the TC genesis month from any of the 19 available years and combined with the extracted surge levels to obtain a 72-h storm tide levels time series. Third, the highest storm tide level was extracted. This procedure was repeated 1000 times, resulting in 1000 maximum storm tide levels per surge peak. Last, we computed the empirical exceedance probabilities of TC storm tides.

For ETCs, a complete year of ETC surge levels, from January 1 until December 31, was combined with year-long tidal levels[91]. The tidal levels time series were randomly shifted between 30 days to include the full spring and neap tide cycle. Second, all storm tide peaks exceeding the smallest tidal level of 19 yearly tidal maxima, which are at least 72-h apart to ensure independent events, were extracted. We repeated this 1000 times to obtain the equivalent of 38,000 years of storm tide time series per output location. Last, we computed the empirical exceedance probabilities of ETC storm tides.

Storm tide RPs were obtained per output location by taking the inverse of the sum of the TC and ETC storm tide yearly exceedance frequency similar to ref. [14]. For a given storm tide level x, we calculated its return period as follows:

$$\mathrm{RP}(x) = \frac{1}{\frac{1}{\mathrm{RP}_{\mathrm{TC}}(x)} + \frac{1}{\mathrm{RP}_{\mathrm{ETC}}(x)}} \quad (1)$$

where RP is the return period in years of storm tide level x. RP_{TC} and RP_{ETC} refer to the return period of the TC and ETC storm tides at the same storm tide level, respectively. At output locations not affected by TCs, Eq. (1) simplifies to $RP = RP_{ETC}$. Throughout the paper, variables like RP100 denote the 100-year RP. This is because it is the storm tide level that is exceeded, on average, once every 100 years, and has an exceedance probability of 0.01 (1/100) in any given year. The EVA method presented here cannot assume storm surge levels exceeding the ones present in the input data[92]. This assumption could lead to an underestimation of ETC storm tide RPs. To test whether this was the case, we compared our empirical approach with fitting extreme value distributions like Gumbel. The results did not show an underestimation of ETC storm tide RPs (Supplementary Fig. 5; Supplementary Note 1). Therefore, we chose to apply the empirical EVA method.

Modeling inundation and flood exposure. To demonstrate a first application of the COAST-RP dataset we computed flood exposure. We developed flood maps for the RP1000 storm tide level using a static inundation model that considers water level attenuation[48]. The multi-error-removed improved-terrain digital elevation model (MERIT DEM)[45] at a 30-arcsecond resolution (approximately 1 km at the equator) was used as input. To account for surface roughness that reduces the water level inland[93], a water level attenuation factor of 0.5 m km^{-1} was used. All areas with a direct connection to the sea and that have an elevation lower than the water level that is reduced by the attenuation factor were inundated. Flood exposure was measured in terms of the exposed population using the Gridded Population of the World version 4 (GPWv4)[46] population count maps for the year 2020. They have been nationally adjusted to data from the United Nations World Population Prospects 2015 Revision[94]. To test the sensitivity of the exposure estimates to the population count maps, we also calculated the exposed population using WorldPop[95] population count maps, which resulted in a 10% reduction of the TC and ETC exposure estimates. Flood protection was not included in the analysis and would lead to an overestimation of the exposed population in areas protected against RP1000 flood events. That said, the flood extent could be underestimated in deltas and estuaries where the river may propagate the storm tide into the hinterland.

Data availability

The COAST-RP dataset developed and applied during the study is available in the 4TU. ResearchData data repository[96] (https://doi.org/10.4121/13392314) and includes storm tide levels with 1, 2, 5, 10, 25, 50, 100, 250, 500, and 1000-year RPs.

Code availability

The TC placing algorithm and the Holland parametric wind model used to generate TC wind fields, written in Python, are available on github: https://github.com/nlesc-mosaic/TCM (TC placing algorithm); https://github.com/NBloemendaal/STORM-return-periods (Holland parametric wind model). Other codes used to generate results reported in the paper and central to its main claims are available upon request from the authors.

Received: 8 January 2021; Accepted: 10 June 2021;
Published online: 29 June 2021

References

1. Storch, H. & Woth, K. Storm surges: perspectives and options. *Sustain. Sci.* **3**, 33–43 (2008).
2. Kulp, S. A. & Strauss, B. H. New elevation data triple estimates of global vulnerability to sea-level rise and coastal flooding. *Nat. Commun.* **10**, 1–12 (2019).
3. Koks, E. E. et al. A global multi-hazard risk analysis of road and railway infrastructure assets. *Nat. Commun.* **10**, 1–11 (2019).
4. Hinkel, J. et al. The ability of societies to adapt to twenty-first-century sea-level rise. *Nat. Clim. Chang.* **8**, 570–578 (2018).
5. Avila, L. A., Stewart, S. R., Berg, R. & Hagen, A. B. *Tropical cyclone report: Hurricane Dorian*. (National Hurricane Center, 2020).
6. Beven, J. L., Berg, R. & Hagen, A. *Tropical Cyclone Report: Hurricane Michael*. (National Hurricane Center, 2019).

7. Deutschländer, T., Friedrich, K., Haeseler, S. & Lefebvre, C. *Severe storm XAVER across northern Europe from 5 to 7 December 2013. Deutscher Wetterdienst* https://www.dwd.de/EN/ourservices/specialevents/storms/20131230_XAVER_europe_en.pdf?__blob=publicationFile&v=4 (2013).
8. Kendon, M. *Storm Ciara. Met Office National Climate Information Centre* https://www.meteo.be/nl/info/nieuwsoverzicht/storm-ciara (2020).
9. Knapp, K. R., Kruk, M. C., Levinson, D. H., Diamond, H. J. & Neumann, C. J. The international best track archive for climate stewardship (IBTrACS): Unifying tropical cyclone best track data. *Bull. Am. Meteorol. Soc.* **91**, 363–376 (2010).
10. Haigh, I. D. et al. Estimating present day extreme water level exceedance probabilities around the coastline of Australia: tides, extra-tropical storm surges and mean sea level. *Clim. Dyn.* **42**, 121–138 (2014).
11. Haigh, I. D. et al. Estimating present day extreme water level exceedance probabilities around the coastline of Australia: tropical cyclone-induced storm surges. *Clim. Dyn.* **42**, 139–157 (2014).
12. Zhang, H. & Sheng, J. Examination of extreme sea levels due to storm surges and tides over the northwest Pacific Ocean. *Cont. Shelf Res.* **93**, 81–97 (2015).
13. Lin, N., Emanuel, K. A., Smith, J. A. & Vanmarcke, E. Risk assessment of hurricane storm surge for New York City. *J. Geophys. Res. Atmos.* **115**, 1–11 (2010).
14. Orton, P. M. et al. A validated tropical-extratropical flood hazard assessment for New York Harbor. *J. Geophys. Res. Ocean.* **121**, 8904–8929 (2016).
15. Wahl, T. et al. Understanding extreme sea levels for broad-scale coastal impact and adaptation analysis. *Nat. Commun.* **8**, 1–12 (2017).
16. Arns, A., Wahl, T., Haigh, I. D., Jensen, J. & Pattiaratchi, C. Estimating extreme water level probabilities: a comparison of the direct methods and recommendations for best practise. *Coast. Eng.* **81**, 51–66 (2013).
17. Aerts, J. C. J. H. et al. Evaluating flood resilience strategies for coastal megacities. *Science* **344**, 473–475 (2014).
18. Muis, S., Verlaan, M., Winsemius, H. C., Aerts, J. C. J. H. & Ward, P. J. A global reanalysis of storm surges and extreme sea levels. *Nat. Commun.* **7**, 1–12 (2016).
19. Vousdoukas, M. I. et al. Global probabilistic projections of extreme sea levels show intensification of coastal flood hazard. *Nat. Commun.* **9**, 2360 (2018).
20. Vafeidis, A. T. et al. A new global coastal database for impact and vulnerability analysis to sea-level rise. *J. Coast. Res.* **24**, 917–924 (2008).
21. Schuerch, M. et al. Future response of global coastal wetlands to sea-level rise. *Nature* **561**, 231–234 (2018).
22. Jongman, B., Ward, P. J. & Aerts, J. C. J. H. Global exposure to river and coastal flooding: Long term trends and changes. *Glob. Environ. Chang* **22**, 823–835 (2012).
23. Hinkel, J. et al. Coastal flood damage and adaptation costs under 21st century sea-level rise. *Proc. Natl Acad. Sci. USA* **111**, 3292–3297 (2014).
24. Hinkel, J. & Klein, R. J. T. Integrating knowledge to assess coastal vulnerability to sea-level rise: the development of the DIVA tool. *Glob. Environ. Chang* **19**, 384–395 (2009).
25. Tiggeloven, T. et al. Global-scale benefit-cost analysis of coastal flood adaptation to different flood risk drivers using structural measures. *Nat. Hazards Earth Syst. Sci.* **20**, 1025–1044 (2020).
26. Muis, S. et al. A high-resolution global dataset of extreme sea levels, tides, and storm surges, including future projections. *Front. Mar. Sci.* **7**, 263 (2020).
27. Vitousek, S. et al. Doubling of coastal flooding frequency within decades due to sea-level rise. *Sci. Rep.* **7**, 1–9 (2017).
28. Bloemendaal, N. et al. Generation of a global synthetic tropical cyclone hazard dataset using STORM. *Sci. Data* **7**, 1–12 (2020).
29. Weinkle, J., Maue, R. & Pielke, R. Historical global tropical cyclone landfalls. *J. Clim.* **25**, 4729–4735 (2012).
30. Pugh, D. T. & Woodworth, P. L. *Sea-Level Science: Understanding Tides, Surges, Tsunamis And Mean Sea-level Changes*. (Cambridge University Press, Cambridge, New York, 2014).
31. Dullaart, J. C. M., Muis, S., Bloemendaal, N. & Aerts, J. C. J. H. Advancing global storm surge modelling using the new ERA5 climate reanalysis. *Clim. Dyn.* **54**, 1007–1021 (2020).
32. Vickery, P. J., Skerlj, P. F. & Twisdale, L. A. Simulation of hurricane risk in the U.S. using empirical track model. *J. Struct. Eng.* **126**, 1222–1237 (2000).
33. Hardy, T. A., McConochie, J. D. & Mason, L. B. Modeling tropical cyclone wave population of the Great Barrier Reef. *J. Waterw. Port Coast. Ocean Eng.* **129**, 104–113 (2003).
34. James, M. K. & Mason, L. B. Synthetic tropical cyclone database. *J. Waterw. Port Coast. Ocean Eng.* **131**, 181–192 (2005).
35. Marsooli, R., Lin, N., Emanuel, K. & Feng, K. Climate change exacerbates hurricane flood hazards along US Atlantic and Gulf Coasts in spatially varying patterns. *Nat. Commun.* **10**, 1–9 (2019).
36. Lin, N. & Emanuel, K. Grey swan tropical cyclones. *Nat. Clim. Chang.* **6**, 106–111 (2016).
37. Emanuel, K., Ravela, S., Vivant, E. & Risi, C. A statistical deterministic approach to hurricane risk assessment. *Bull. Am. Meteorol. Soc.* **87**, 299–314 (2006).
38. Lee, C. Y., Tippett, M. K., Sobel, A. H. & Camargo, S. J. An environmentally forced tropical cyclone hazard model. *J. Adv. Model. Earth Syst.* **10**, 223–241 (2018).
39. Muis, S. et al. Spatiotemporal patterns of extreme sea levels along the western North-Atlantic coasts. *Sci. Rep.* **9**, 1–12 (2019).
40. Rodwell, M. J. & Hoskins, B. J. Subtropical anticyclones and summer monsoons. *J. Clim.* **14**, 3192–3211 (2001).
41. Emanuel, K. A. & Rotunno, R. Polar lows as arctic hurricanes. *Tellus A Dyn. Meteorol. Oceanogr.* **41**, 1–17 (1989).
42. Dolan, R. & Davis, R. Coastal storm hazards. *J. Coast. Res.* 103–114 (1994).
43. New York City Panel on Climate Change. Climate risk information 2013: Observations, climate change projections, and maps. (eds Rosenzweig, C. & Solecki, W.) NPCC2. Prepared for use by the City of New York Special Initiative on Rebuilding and Resiliancy, (New York, NY, 2013).
44. Rasmussen, D. J., Buchanan, M. K., Kopp, R. E. & Oppenheimer, M. A flood damage allowance framework for coastal protection with deep uncertainty in sea level rise. *Earth's Futur.* **8**, e2019EF001340 (2020).
45. Yamazaki, D. et al. A high-accuracy map of global terrain elevations. *Geophys. Res. Lett.* **44**, 5844–5853 (2017).
46. CIESIN. Gridded population of the world, Version 4 (GWPv4): Population count adjusted to match 2015 revision of UN WPP country totals, revision 11. *Palisades, NY: NASA Socioecnomic Data and Applications Center (SEDAC).* https://doi.org/10.7927/H4PN93PB. (2018).
47. Scussolini, P. et al. FLOPROS: an evolving global database of flood protection standards. *Nat. Hazards Earth Syst. Sci.* **16**, 1049–1061 (2016).
48. Ward, P. J. et al. *Aqueduct Floods Methodology. World Resources Institute: Technical Note* www.wri.org/publication/aqueduct-floods-methodology (2020).
49. Feng, J., Li, D., Li, Y., Liu, Q. & Wang, A. Storm surge variation along the coast of the Bohai Sea. *Sci. Rep.* **8**, 1–10 (2018).
50. Holland, G. J. An analytic model of the wind and pressure profiles in hurricanes. *Mon. Weather Rev.* **108**, 1212–1218 (1980).
51. Holland, G. J., Belanger, J. I. & Fritz, A. A revised model for radial profiles of hurricane winds. *Mon. Weather Rev.* **138**, 4393–4401 (2010).
52. Musinguzi, A., Akbar, M. K., Fleming, J. G. & Hargrove, S. K. Understanding hurricane storm surge generation and propagation using a forecasting model, forecast advisories and best track in a wind model, and observed data—case study hurricane Rita. *J. Mar. Sci. Eng.* **7**, 77 (2019).
53. Knaff, J. A., Kossin, J. P. & DeMaria, M. Annular hurricanes. *Weather Forecast* **18**, 204–223 (2003).
54. Lin, N. & Chavas, D. On hurricane parametric wind and applications in storm surge modeling. *J. Geophys. Res.* **117**, 19 (2012).
55. Emanuel, K. & Rotunno, R. Self-stratification of tropical cyclone outflow. Part I: implications for storm structure. *J. Atmos. Sci.* **68**, 2236–2249 (2011).
56. Hu, K., Chen, Q. & Kimball, S. K. Consistency in hurricane surface wind forecasting: an improved parametric model. *Nat. Hazards* **61**, 1029–1050 (2012).
57. Chavas, D. R., Lin, N. & Emanuel, K. A model for the complete radial structure of the tropical cyclone wind field. Part I: Comparison with observed structure. *J. Atmos. Sci.* **72**, 3647–3662 (2015).
58. Horsburgh, K. J. & Wilson, C. Tide-surge interaction and its role in the distribution of surge residuals in the North Sea. *J. Geophys. Res. Ocean.* **112**, C08003 (2007).
59. Santamaria-Aguilar, S. & Vafeidis, A. T. Are extreme skew surges independent of high water levels in a mixed semidiurnal tidal regime? *J. Geophys. Res. Ocean.* **123**, 8877–8886 (2018).
60. Arns, A. et al. Non-linear interaction modulates global extreme sea levels, coastal flood exposure, and impacts. *Nat. Commun.* **11**, 1–9 (2020).
61. Stewart, R. H. *Introduction to Physical Oceanography*. (Department of Oceanography, Texas A and M University, 2008). https://doi.org/10.1119/1.18716.
62. Kirezci, E. et al. Projections of global-scale extreme sea levels and resulting episodic coastal flooding over the 21st century. *Sci. Rep.* **10**, 1–12 (2020).
63. Trinh, T. T., Pattiaratchi, C. & Bui, T. The contribution of Forerunner to storm surges along the Vietnam Coast. *J. Mar. Sci. Eng.* **8**, 508 (2020).
64. Eliot, M. & Pattiaratchi, C. Remote forcing of water levels by tropical cyclones in Southwest Australia. *Cont. Shelf Res.* **30**, 1549–1561 (2010).
65. Muis, S., Haigh, I. D., Guimarães Nobre, G., Aerts, J. C. J. H. & Ward, P. J. Influence of El Niño-Southern Oscillation on Global Coastal Flooding. *Earth's Futur.* **6**, 1311–1322 (2018).
66. Rashid, M. M., Wahl, T., Chambers, D. P., Calafat, F. M. & Sweet, W. V. An extreme sea level indicator for the contiguous United States coastline. *Sci. Data* **6**, 1–14 (2019).
67. Knutson, T. et al. Tropical cyclones and climate change assessment. Part II: Projected response to anthropogenic warming. *Bull. Am. Meteorol. Soc.* **101**, 303–322 (2020).
68. Kossin, J. P. A global slowdown of tropical-cyclone translation speed. *Nature* **558**, 104–107 (2018).

69. Baatsen, M., Haarsma, R. J., Van Delden, A. J. & de Vries, H. Severe autumn storms in future western Europe with a warmer Atlantic Ocean. *Clim. Dyn.* **45**, 949–964 (2015).
70. Michaelis, A. C., Willison, J., Lackmann, G. M. & Robinson, W. A. Changes in winter North Atlantic extratropical cyclones in high-resolution regional pseudo-global warming simulations. *J. Clim.* **30**, 6905–6925 (2017).
71. Coles, S. *An Introduction to Statistical Modeling of Extreme Values. Springer Series in Statistics* (Springer London, 2001).
72. Irazoqui Apecechea, M., Verlaan, M., Zijl, F., Le Coz, C. & Kernkamp, H. Effects of self-attraction and loading at a regional scale: a test case for the Northwest European shelf. *Ocean Dyn.* **67**, 729–749 (2017).
73. Kernkamp, H. W. J., Van Dam, A., Stelling, G. S. & de Goede, E. D. Efficient scheme for the shallow water equations on unstructured grids with application to the Continental Shelf. *Ocean Dyn.* **61**, 1175–1188 (2011).
74. Pugh, D. T. *Tides, Surges and Mean Sea-level (Reprinted with corrections).* (John Wiley & Sons, Ltd., 1996).
75. Zweers, N. C., Makin, V. K., de Vries, J. W. & Burgers, G. On the influence of changes in the drag relation on surface wind speeds and storm surge forecasts. *Nat. Hazards* **62**, 207–219 (2012).
76. Hardy, T., Mason, L. & Astorquia, A. *Queensland Climate Change and Community Vulnerability to Tropical Cyclones-Ocean Hazards Assessment-Stage 3: the Frequency of Surge plus Tide during Tropical Cyclones for Selected Open Coast Locations along the Queensland East Coast*. https://doi.org/10.13140/RG.2.1.4856.5928. (2004).
77. Chertova, M., Muis, S., Pelupessy, I. & Ward, P. Incorporating large datasets of synthetic tropical cyclones with Global Tide and Surge Model (GTSM) for global assessment of extreme sea levels. In *22nd EGU General Assembly* EGU2020-21189, https://doi.org/10.5194/egusphere-egu2020-21189 (2020).
78. Chavas, D. R. & Emanuel, K. A. A QuikSCAT climatology of tropical cyclone size. *Geophys. Res. Lett.* **37**, L18816 (2010).
79. Kalourazi, M. Y., Siadatmousavi, S. M., Yeganeh-Bakhtiary, A. & Jose, F. Simulating tropical storms in the Gulf of Mexico using analytical models. *Oceanologia* **62**, 173–189 (2019).
80. Batts, M. E., Cordes, M. R., Russel, L. R., Shaver, J. R. & Simiu, E. Hurricane wind speeds in the United States. *NBS Build. Sci. Ser.* **124**, 50 (1980).
81. Harper, B. A., Kepert, J. D. & Ginger, J. D. *Guidelines for Converting between Various Wind Averaging in Tropical Cyclone Conditions*. https://library.wmo.int/doc_num.php?explnum_id=290 (2010).
82. Queensland Government. *Queensland Climate Change and Community Vulnerability to Tropical Cyclones: Ocean Hazards Assessment-stage 1*. http://www.systemsengineeringaustralia.com.au/download/Ocean_Hazards_Assess_Stage1A_revised.pdf (2001).
83. Garratt, J. R. Review of drag coefficients over oceans and continents. *Mon. Weather Rev.* **105**, 915–929 (1977).
84. Westerink, J. J. et al. A basin- to channel-scale unstructured grid hurricane storm surge model applied to southern Louisiana. *Mon. Weather Rev.* **136**, 833–864 (2008).
85. Powell, M. D., Vickery, P. J. & Reinhold, T. A. Reduced drag coefficient for high wind speeds in tropical cyclones. *Nature* **422**, 279–283 (2003).
86. Sterl, A. *Drag at high wind velocities-a review, Technical Report. TR-361*. http://projects.knmi.nl/publications/fulltexts/sterl_review_drag_tr361_2017.pdf (2017).
87. Nederhoff, K., Giardino, A., Van Ormondt, M. & Vatvani, D. Estimates of tropical cyclone geometry parameters based on best-track data. *Nat. Hazards Earth Syst. Sci.* **19**, 2359–2370 (2019).
88. Hersbach, H. et al. Global reanalysis: goodbye ERA-Inteirm, hello ERA5. *ECMWF Newsl* **159**, 17–24 (2019).
89. Charnock, H. Wind stress on a water surface. *Q. J. R. Meteorol. Soc.* **81**, 639–640 (1955).
90. Bryant, K. M. & Akbar, M. An exploration of wind stress calculation techniques in hurricane storm surge modeling. *J. Mar. Sci. Eng.* **4**, 58 (2016).
91. Goring, D. G., Stephens, S. A., Bell, R. G. & Pearson, C. P. Estimation of extreme sea levels in a tide-dominated environment using short data records. *J. Waterw. Port Coast. Ocean Eng.* **137**, 150–159 (2011).
92. Fortunato, A. B., Li, K., Bertin, X., Rodrigues, M. & Miguez, B. M. Determination of extreme sea levels along the Iberian Atlantic coast. *Ocean Eng.* **111**, 471–482 (2016).
93. Vafeidis, A. T. et al. Water-level attenuation in broad-scale assessments of exposure to coastal flooding: a sensitivity analysis. *Nat. Hazards Earth Syst. Sci.* **19**, 973–984 (2019).
94. U. N. United Nations, Department of Economic and Social Affairs, Population Divison. *World Population Prospects: The 2015 Revision*. https://population.un.org/wpp/ (2015).
95. Tatem, A. J. WorldPop, open data for spatial demography. *Sci. Data* **4**, 1–4 (2017).
96. Dullaart, J. C. M. et al. COAST-RP: A global COastal dAtaset of Storm Tide Return Periods. *4TU.ResearchData*. https://doi.org/10.4121/13392314. (2021).

Acknowledgements

We would like to thank Martin Verlaan and Maialen Irazoqui Apecechea from Deltares for their support with the use of GTSM. The authors also acknowledge Arne Arns for sharing his thoughts on the statistical analysis. We would also like to thank Ivan Haigh and Reza Marsooli for providing validation data. We thank Maxime Moge from SURFsara (http://www.surfsara.nl) for his support in using the Cartesius Computer Cluster. J.D. received funding from the COASTRISK project financed by the SCOR Corporate Foundation for Science (R/003316.01). S.M. and M.C. received funding from the research program MOSAIC with project number ASDI.2018.036, which is financed by the NWO. N.B. and J.A. are funded by a VICI grant from the Netherlands Organization for Scientific Research (NWO) (Grant Number 453-13-006) and the ERC Advanced Grant COASTMOVE #884442. A.C. was supported by the Dutch Research Council (NWO) (VIDI; grant no. 016.161.324). This work was sponsored by NWO Exact and Natural Sciences for the use of supercomputer facilities (grant no. 2020.007).

Author contributions

J.D. performed the hydrodynamic modeling and analysis and wrote the paper. S.M. carried out the inundation modeling, M.C. developed the tropical cyclone placing algorithm, and A.C. assisted in the statistical analysis. N.B. and J.A. participated in technical discussions and all authors co-wrote the paper.

Competing interests

The authors declare no competing interests.

Additional information

Supplementary information The online version contains supplementary material available at https://doi.org/10.1038/s43247-021-00204-9.

Correspondence and requests for materials should be addressed to J.C.M.D.

Peer review information Communications Earth & Environment thanks the anonymous reviewers for their contribution to the peer review of this work. Primary Handling Editors: Adam Switzer and Joe Aslin. Peer reviewer reports are available.

Reprints and permission information is available at http://www.nature.com/reprints

Publisher's note Springer Nature remains neutral with regard to jurisdictional claims in published maps and institutional affiliations.